

pubs.acs.org/JACS Article

Tailoring Electronic and Optical Properties of MXenes through Forming Solid Solutions

Meikang Han,^{\$} Kathleen Maleski,^{\$} Christopher Eugene Shuck,^{\$} Yizhou Yang, James T. Glazar, Alexandre C. Foucher, Kanit Hantanasirisakul, Asia Sarycheva, Nathan C. Frey, Steven J. May, Vivek B. Shenoy, Eric A. Stach, and Yury Gogotsi*



Cite This: J. Am. Chem. Soc. 2020, 142, 19110-19118



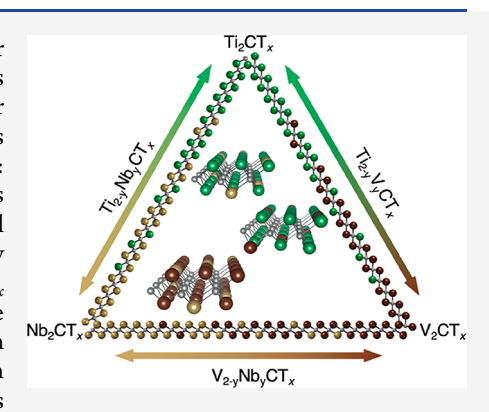
ACCESS

Metrics & More

Article Recommendations

s Supporting Information

ABSTRACT: Alloying is a long-established strategy to tailor properties of metals for specific applications, thus retaining or enhancing the principal elemental characteristics while offering additional functionality from the added elements. We propose a similar approach to the control of properties of two-dimensional transition metal carbides known as MXenes. MXenes $(M_{n+1}X_n)$ have two sites for compositional variation: elemental substitution on both the metal (M) and carbon/nitrogen (X) sites presents promising routes for tailoring the chemical, optical, electronic, or mechanical properties of MXenes. Herein, we systematically investigated three interrelated binary solid-solution MXene systems based on Ti, Nb, and/or V at the M-site in a M_2XT_x structure $(Ti_{2-y}Nb_yCT_x$, $Ti_{2-y}V_yCT_x$, and $V_{2-y}Nb_yCT_x$, where T_x stands for surface terminations) showing the evolution of electronic and optical properties as a function of composition. All three MXene systems show unlimited solubility and random distribution of metal elements in the metal sublattice. Optically, the MXene systems



are tailorable in a nonlinear fashion, with absorption peaks from ultraviolet to near-infrared wavelength. The macroscopic electrical conductivity of solid solution MXenes can be controllably varied over 3 orders of magnitude at room temperature and 6 orders of magnitude from 10 to 300 K. This work greatly increases the number of nonstoichiometric MXenes reported to date and opens avenues for controlling physical properties of different MXenes with a limitless number of compositions possible through M-site solid solutions.

INTRODUCTION

Since the Bronze age, alloying has been utilized to improve properties of metals by combining elements into solid solutions. Similar to metal alloys, substitution of one metal with another is possible in the structure of many inorganic compounds, such as nitrides, carbides, borides, oxides, or transition metal dichalcogenides, leading to the formation of solid solutions. 1,2 This approach presents limitless possibilities to tune the chemical and physical properties, such as bandgap, electrocatalytic activity, piezoelectricity, mechanical properties, and others, purely through the control of chemical composition without changing the crystal structure.3-5 For example, atomically thin two-dimensional (2D) MoS_{2y}Se_{2(1-y)} and $Mo_{\nu}W_{1-\nu}S_2$ nanosheets were synthesized over their complete range of respective compositions $(0 \le y \le 1)$, producing tunable photoluminescence. 6 Continuous solid solutions are known to form in many transition metal carbide systems.⁷⁻⁹ This is an efficient approach to diversify and control intrinsic physicochemical characteristics with composition engineering for practical applications.

MAX phases are a class of layered ceramics that show a combination of ceramic and metallic characteristics. ¹⁰ The general formula is $M_{n+1}AX_n$ (n = 1-4), where M is an early

transition metal element (Ti, V, Nb, Cr, etc.), A is typically a group 13 or 14 element (Al, Si, Ge, Ga, etc.), and X is C and/ or N. Over 150 discrete MAX phases currently exist, ¹¹ but the fact that all three sites (M, A, and/or X) can achieve distinct occupancies by multiple elements leads to the possibility of a theoretically infinite number of solid-solution MAX phases. To date, many single-site solid-solution MAX phases have been studied computationally and experimentally, such as $Cr_{2-x}V_xAlC$, $V_2(Sn,A)C$ (A = Fe, Co, Ni, Mn), $Ti_3Al(C,N)_2$, and many others. ¹²⁻¹⁵ The diversity of solid-solution MAX phases offers the opportunity to tune their specific properties by controlling the chemical composition. For example, the compressive strength of Ti_2AlC has been improved by substituting Ti with V to form $Ti_{2-x}V_xAlC$ solid solutions. ¹⁶ In addition, it has been demonstrated that ferromagnetism can

Received: July 9, 2020 Published: October 27, 2020





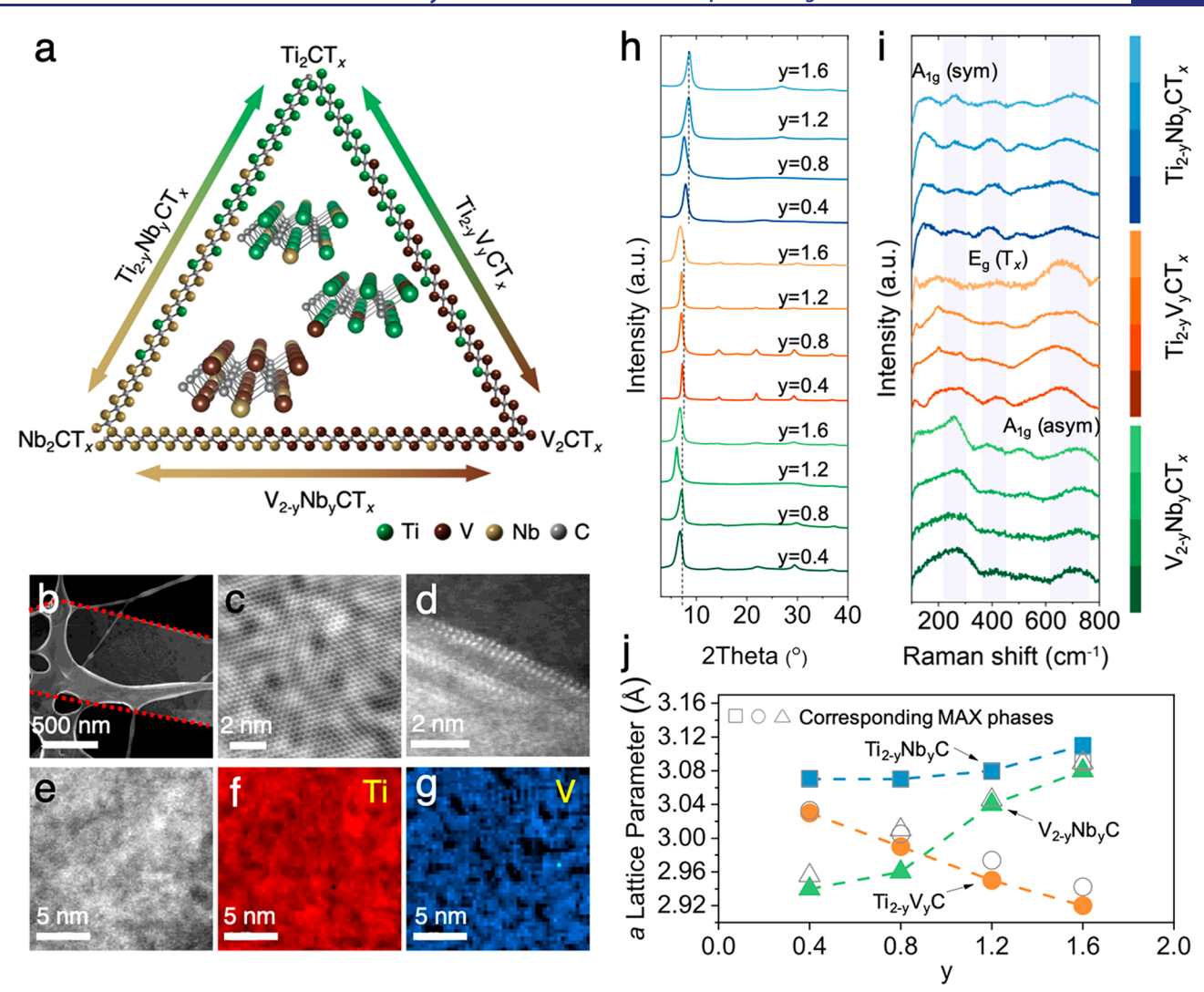


Figure 1. Characterization of solid-solution $M'_{2-y}M''_yCT_x$ MXenes. (a) The compositional triangle of $Ti_{2-y}Nb_yCT_x$, $Ti_{2-y}V_yCT_{x}$, and $V_{2-y}Nb_yCT_x$ showing the continuous solid solutions of M_2C -type MXenes. The double arrows illustrate the color evolution of solid-solution MXene films with the M-site composition change. Insets are the atomic structures of bare solid-solution MXenes showing the metal element arrangement used for DFT calculations. (b) STEM image of a $Ti_{1.2}V_{0.8}CT_x$ MXene flake showing the typical size and shape of the MXene flakes produced in this work. (c) Fourier filtered dark-field STEM image of a $Ti_{1.2}V_{0.8}CT_x$ flake along the [001] zone axis. (d) Cross-sectional STEM image of a $Ti_{1.2}V_{0.8}CT_x$ flake showing the two layers of bright atoms (Ti/V layers). (e, f, g) STEM EDS mapping of a $Ti_{1.2}V_{0.8}CT_x$ MXene showing the random distribution of Ti and V. (h) XRD patterns of all MXene films studied in the work, showing the delaminated layers. (i) Raman spectra of all of the MXene films showing the vibration change with varied composition. (j) The calculated a lattice parameters of bare $M'_{2-y}M''_yC$ MXenes, matching well with those of the corresponding MAX phases.

be introduced in solid-solution MAX phases by alloying magnetic elements in M site. 17

MXenes, a rapidly expanding family of 2D materials, are topochemically synthesized through selective etching of the A element from MAX phases. 18,19 Consequently, their general formula is $M_{n+1}X_nT_x$ (n=1-4), where T_x represents the surface terminations (=O, –OH, –F, –Cl, etc.). Given the fact that MXenes are typically derived from MAX phases or related layered precursors, inheriting the composition and structure of carbide/nitride layers of the precursor, it is possible to obtain solid-solution MXenes from the corresponding MAX phases through substitution in M and/or X sites. To date, multiple-M solid-solution MXenes have been synthesized as $(M',M'')_2XT_x$ $(M',M'')_3X_2T_x$ and $(M',M'')_4X_3T_x$ structures with the following compositions: $(Ti,V)_2CT_x$ $TiNbCT_x$ $Ti_{1.5}V_{1.5}C_2T_x$ $(V_{0.5},Cr_{0.5})_3C_2T_x$ $(Mo,V)_4C_3T_x$ $Nb_{3.2}Zr_{0.8}C_3T_x$ and $Nb_{3.2}Ti_{0.8}C_3T_x$. However, no systematic studies over

the complete range of compositions have been reported, and no composition-property relations have been established for solid-solution MXenes. The effects of solid solution composition on the elemental distribution and intrinsic MXene characteristics remain unexplored. Owing to their metallic conductivity, tunable surface chemistry, hydrophilicity, and scalability, MXenes have found widespread use in a variety of fields, including energy storage, gas sensors, antennas, catalysis, and electromagnetic interference (EMI) shielding. Precise tailoring of the properties of MXenes by control of their compositions could improve their performance in applications previously investigated as well as open new areas of use for MXenes.

Herein, we systematically investigated an interrelated group of three solid-solution MXene systems, consisting of 12 $M'_{2-y}M''_{y}XT_{x}$ compositions $(Ti_{2-y}Nb_{y}CT_{x})$ $Ti_{2-y}V_{y}CT_{x}$, and $V_{2-y}Nb_{y}CT_{x})$ forming continuous solid solutions on M-site

(Figure 1a), to explore the relationship between the composition and the structural, electronic, and optical properties of MXenes. The structure of both the precursor MAX phases and their respective MXenes are analyzed. Density functional theory (DFT) calculations and X-ray absorption spectroscopy (XAS) are conducted to provide an understanding of the correlation between the composition and electronic structure. The absorption spectra were recorded in the ultraviolet-visible (UV-vis) wavelength range of 200-1000 nm, and the electrical resistivity was measured from 10 to 300 K for each system. This work points to the possibility of synthesizing a limitless number of new MXene compositions by substitution of the transition metal for enhanced control over the MXene properties, enabling them to be tailored for particular applications, such as EMI shielding, energy storage, sensors, or electrochromic films.

■ RESULTS AND DISCUSSION

Three solid-solution MXene systems (Ti_{2-y}Nb_yCT_x, $Ti_{2-v}V_{\nu}CT_{x\nu}$ and $V_{2-v}Nb_{\nu}CT_{x\nu}$; y = 0.4, 0.8, 1.2, and 1.6, obtained from the precursor composition) were synthesized using the corresponding MAX phases. To obtain high-quality single-/few-layered MXene flakes for different MXene compositions, different etching and delamination processes were used (details in Supporting Information). For all MAX phases (synthesis information in Supporting Information), Ti_{2-v}Nb_vAlC, Ti_{2-v}V_vAlC, and V_{2-v}Nb_vAlC, the produced phases have only the desired M2AX phase present (Figure S1), with no impurity phases. The characteristic diffraction peaks (002 shown in Figure S1b,e,h, and 110 shown in Figure S1c,f,i) systematically shift with the ratio of M'/M" without broadening or splitting, indicating that the MAX phases have homogeneous chemical composition. All exhibit linear relationships between the chemical composition and their a and c lattice parameters (Figure S2). Energy-dispersive X-ray spectroscopy (EDS) was used to determine the ratio of M'/M" in each MXene (Figure S3), confirming that the stoichiometric values are consistent with the corresponding MAX phases.

All MXenes synthesized in this study were delaminated into single flakes. Here, Ti_{1.2}V_{0.8}CT_x is used as an example to show the crystal structure and elemental arrangement. An electronbeam-transparent 2D flake can be observed in Figure 1b. Figure 1c shows the Fourier filtered dark-field scanning transmission electron microscopy (STEM) image of the flake along the [001] zone axis, indicating the hexagonal symmetry of the planes without visible lattice variation. From the crosssection of the flake, two layers of bright spots which correspond to two metal layers show the M-C-M structure (Figure 1d). High-resolution EDS mapping shows a homogeneous distribution of Ti and V atoms, demonstrating the random arrangement of metal elements (Figure 1e-g). $Ti_{2-v}Nb_vCT_x$ and $V_{2-v}Nb_vCT_x$ MXenes show the same crystal structure and elemental arrangement as Ti_{2-v}V_vCT_r (Figure S4 and S5). Electron energy loss spectroscopy (EELS) measurements of Ti_{2-v}V_vCT_x (Figure S6) indicate that the M-elemental composition is in agreement with the precursor Ti2-vV,AlC, and the elemental distribution is homogeneous. Dynamic light scattering (DLS) of Ti_{2-v}V_vCT_x flakes revealed intensity distribution averages from 140 to 520 nm (Figure S7).

The freestanding films of three solid-solution MXene systems were fabricated using vacuum-assisted filtration. Figure S8 shows that the film colors range from green (Ti_2CT_x) and gold (Nb_2CT_x) to bronze (V_2CT_x) . As shown in X-ray

diffraction (XRD) patterns of all MXene films (Figure 1h), the shift in the 002 peaks from $12.7 \sim 13.5^{\circ}$ (2 θ) to $6.2 \sim 8^{\circ}$ confirms removal of Al layers from all as-synthesized solidsolution MXenes and their delamination into single- to fewlayer flakes. It is noteworthy that different delamination processes lead to varying interlayer spacings. It is apparent that $Ti_{2-v}V_{\nu}CT_{x}$ and $V_{2-v}Nb_{\nu}CT_{x}$ have larger d-spacings than $Ti_{2-y}Nb_yCT_x$. For example, the *d*-spacing of $Ti_{1.2}Nb_{0.8}T_x$ is 11.6 Å while that of $V_{1.2}Nb_{0.8}T_x$ and $Ti_{1.2}V_{0.8}T_x$ is 12.8 Å. Tetramethylammonium hydroxide (TMAOH) was used as an intercalant for $Ti_{2-y}V_yCT_x$ and $V_{2-y}Nb_yCT_x$ while Li^+ contributed to the delamination of Ti2-yNbyCTx. Raman spectra of M2XTx systems, which exhibit 6 Raman-active vibrations, offer an insight into the effect of solid-solution composition on lattice vibrations (Figure 1i). Both mass of the atoms involved in vibration and bond strength affect the position of Raman peaks. The larger mass difference between metals, the larger Raman peak shift is expected. Thus, the Ti_{2-v}Nb_vCT_x system shows the largest peak shift. Here, the symmetric A_{1g} peak (~250–300 cm⁻¹) shifts toward lower wavenumbers with increased amount of the heavier metal (Nb). The trend in the A_{1g} asymmetric vibration (\sim 650–750 cm⁻¹) is not linear for the Ti_{2-y}Nb_yCT_x system. In case of $Ti_{2-y}V_yCT_x$ system, the peak position of A_{1g} vibrations does not change. Instead, the E_g vibrations ($\sim 380-450$ cm⁻¹) of surface groups shift nonlinearly with changing the chemical composition. The shift of Raman vibrations indicates that the lattice parameters of solid-solution MXenes change with the changing composition, verifying the XRD results from the MAX precursors (Figures S1, S2). It is important to note that atomic composition is not the only factor affecting Raman spectra; other factors may also account for the vibrations, such as interlayer spacing, surface terminations, in-plane defects, etc.³³ X-ray photoelectron spectroscopy (XPS) provides details concerning the bonding structure and surface chemistry of Ti_{2-v}Nb_vCT_x (Figure S9), Ti_{2-v}V_vCT_x (Figure S10), and $V_{2-y}Nb_yCT_x$ (Figure S11). For each system, the representative spectra are presented, with quantification of the elemental ratios and surface functional groups (Tables S2 and S3). The calculated ratios of the two metal elements are in agreement with the initial stoichiometric mixture and EDS (Figure S3).

DFT calculations were performed to understand the ordering tendencies and structural properties of the solidsolution MXene systems. In order to simulate the random metal site occupation in MXenes, multiple low-energy solid solution configurations, generated with the MIT Ab-Initio Phase Stability (MAPS) cluster expansion code, were considered (see Supporting Information for computational details).³⁴ An analysis of the effective cluster interactions and predicted structural energies shows that the cluster expansion was well converged and provides insight into the interactions between the elements. The DFT-calculated formation energies of over 150 structures per system show that multiple stable (negative formation energy) solid-solution structures exist for each system (Figure S12). Figure S13 plots the fitted effective cluster interactions against cluster size, displaying a decaying behavior as expected from a converged cluster expansion.³⁴ It also highlights that short-range homometallic interactions are strongly repulsive, encouraging uniform elemental mixing as observed experimentally. The comparison of cluster expansionpredicted and DFT-calculated formation energies illustrates that the fitted cluster expansion accurately reproduces the DFT calculations (Figure S14). Insets in Figure 1a illustrate side-

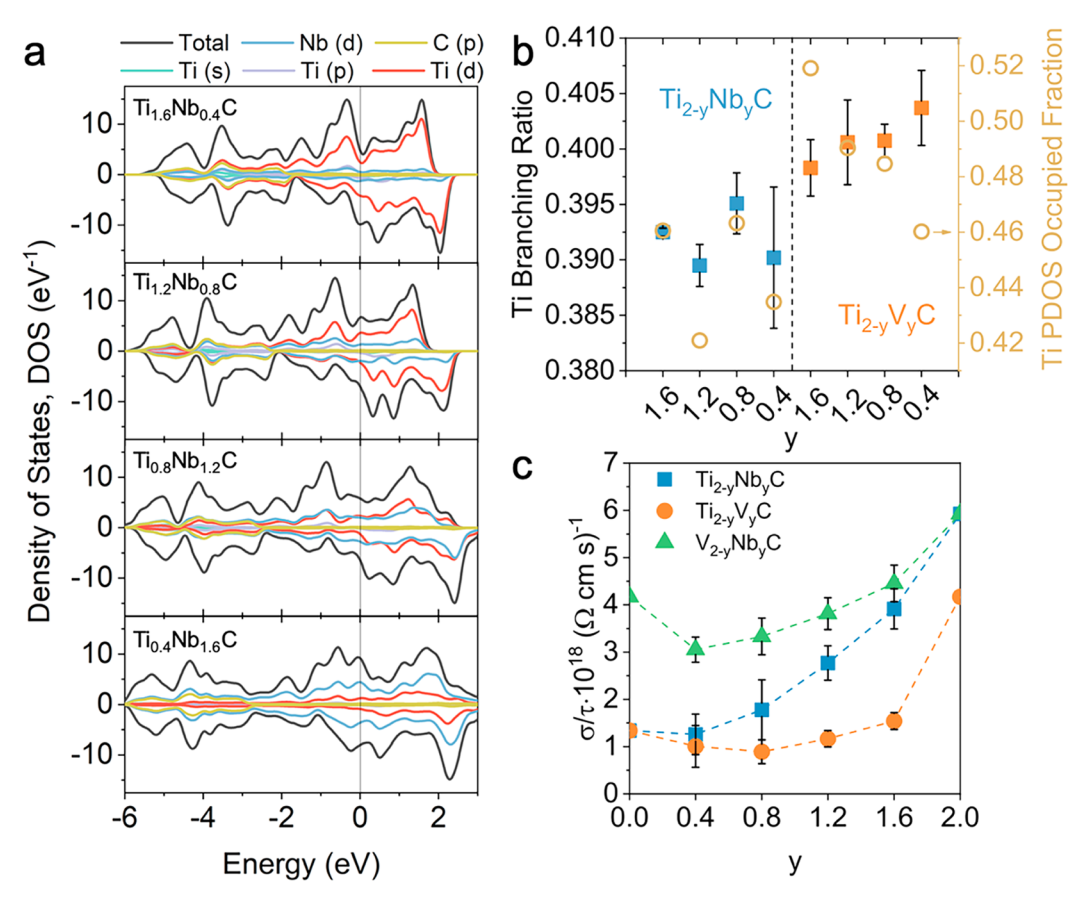


Figure 2. DFT and XAS analysis of electronic structure of solid-solution $M'_{2-y}M''_yCT_x$ MXenes. (a) The computed DOS of bare $Ti_{2-y}Nb_yC$ as an example of solid-solution MXenes, showing the DOS change with substitution in M-site. (b) Ti branching ratios of $Ti_{2-y}Nb_yC$ and $Ti_{2-y}V_yC$ obtained from X-ray absorption spectra, error bars indicate standard deviation of measurements taken at different parts of the same samples; it shows the correspondence with the Ti d-orbital-derived PDOS occupied fractions. (c) The calculated electrical conductivity of bare $M'_{2-y}M''_yC$ MXenes, showing the conductivity change with varying solid solutions.

view atomic structures of bare Ti_{1.6}Nb_{0.4}C, Ti_{1.6}V_{0.4}C, and V_{1.6}Nb_{0.4}C that were determined by the cluster expansion code to be ground states at their respective concentrations. These ground state unit cells were used for detailed lattice parameter and density of states (DOS) calculations, and were included among an ensemble of similar low-energy unit cells to calculate the average conductivity for each solid-solution concentration. Using the lowest-energy structures for each experimentally synthesized solid-solution concentration, the a lattice parameter (a-LP) of bare solid-solution MXenes was calculated (Figure 1j). The predicted a-LP values of MXenes are very close (<1% difference at most) to the a-LP values of the corresponding MAX phases as calculated from the XRD patterns (Figure S2). With an increasing ratio of Nb, the a-LPs of Ti_{2-y}Nb_yC and V_{2-y}Nb_yC increase, while the a-LPs of Ti_{2-v}V_vC decrease with increasing V element. These trends match the a-LPs of the corresponding MAX phases, demonstrating a near linear relationship between a-LP and M-site composition.

We further calculated the electronic structures of bare solid-solution MXenes. As shown in Figure 2a, with the increasing ratio of Nb, the density of Nb d-states increases while the density of Ti d-states decreases near the Fermi level. Moreover, the total DOS of Ti_{2-y}Nb_yC at the Fermi level increases with an increasing ratio of Nb, which is attributed to the increased number of Nb valence electrons over Ti. The DOSs of Ti_{2-y}V_yC (Figure S15a) and V_{2-y}Nb_yC (Figure S15b) systems

show a similar behavior with ${\rm Ti}_{2-y}{\rm Nb}_y{\rm C}$ MXenes. Additionally, a slight ferromagnetic interaction that splits majority and minority spin carriers can be observed. These spin-polarized calculations, performed to enable quicker convergence to the electronic ground state, do not however indicate an appreciable magnetic moment for the bare solid-solution MXenes. Overall, the calculated DOSs indicate that the metallic d-states dominate the electronic behavior near the Fermi level.

To better understand the role of M-site composition on the electronic structure of these MXenes, soft XAS was collected in total electron yield mode at room temperature. Representative XAS spectra for the Ti, V, and Nb L-edges are shown in Figure S16a-c. From our previous XAS studies on Ti-based MXenes, it was found that the $L_{2,3}$ branching ratio is a suitable way to reveal trends in the electron count per metal atom in MXenes.³⁵ Here, the branching ratio is defined as the integrated area under the L_3 absorption peak divided by the total integrated area under the $L_{2,3}$ peak. For Ti and V, the relative d-electron count per atom is determined by the $L_{2,3}$ branching ratio, which increases as the number of occupied electron states increases. 36,37 For Nb, there remain conflicting reports regarding how the branching ratio corresponds to the charge density;³⁸ therefore, we focus analysis on the Ti and V branching ratios. Comparing Ti_{2-v}V_vCT_x and Ti_{2-v}Nb_vCT_x, we find a clear M-site chemistry dependence to the branching ratio, indicating that the Ti band filling is influenced by its M-

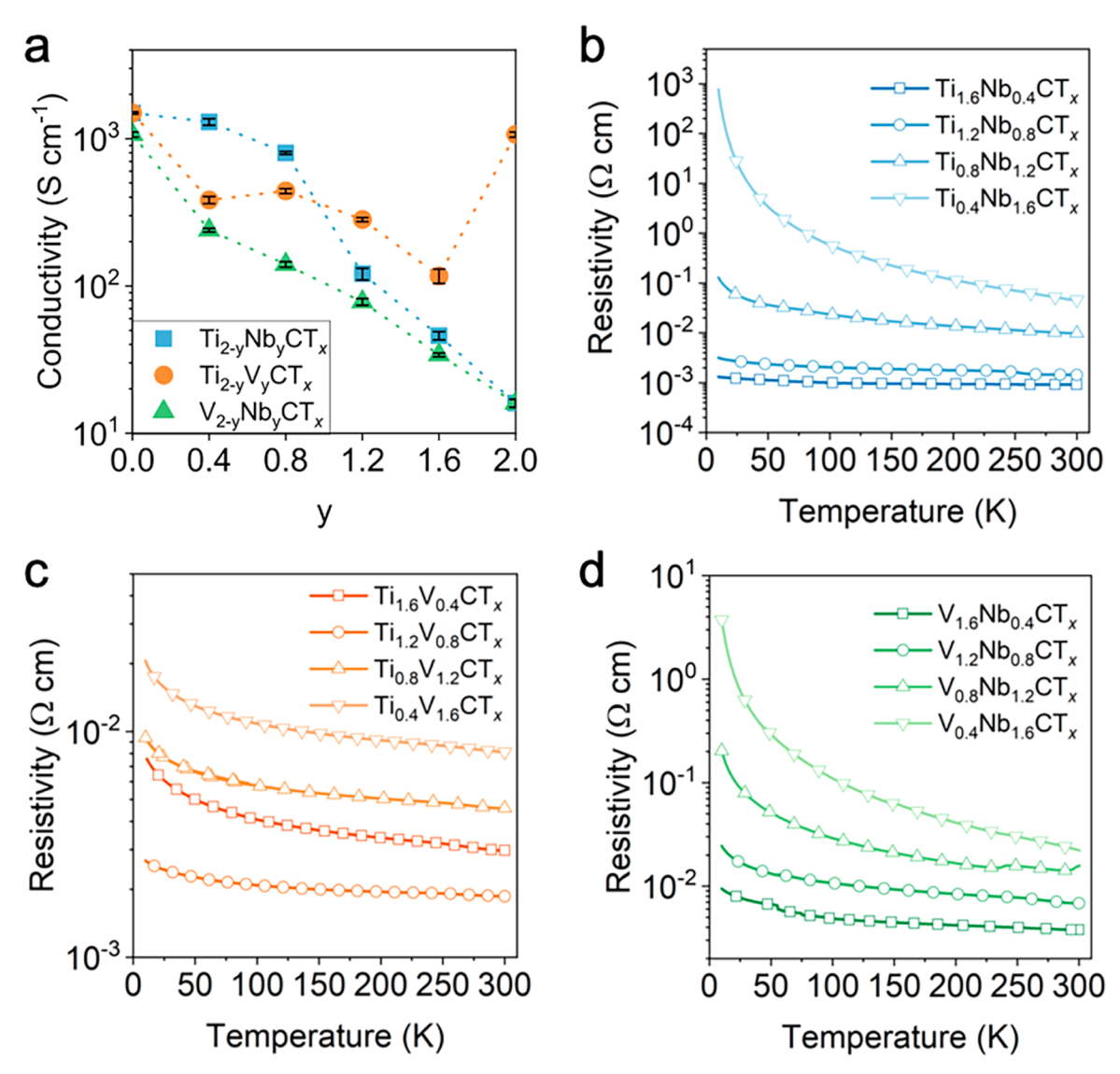


Figure 3. Electronic properties of solid-solution $M'_{2-y}M''_yCT_x$ MXenes. (a) The electrical conductivity of $Ti_{2-y}Nb_yCT_w$ $Ti_{2-y}V_yCT_w$ and $V_{2-y}Nb_yCT_x$ MXenes measured by four-probe method at room temperature showing the conductivity change with varied composition. Temperature dependence of resistivity for (b) $Ti_{2-y}Nb_yCT_w$ (c) $Ti_{2-y}V_yCT_w$ and (d) $V_{2-y}Nb_yCT_x$ MXene films.

site counterpart. In a comparison of the Ti branching ratios in both Ti-containing MXenes, the Ti atoms in $Ti_{2-v}V_{\nu}CT_{\nu}$ have higher electron counts, with an average branching ratio of 0.40, than those in Ti_{2-v}Nb_vCT_x, where the average Ti L-edge branching ratio is 0.39, as shown in Figure 2b. To identify if this electronic trend could arise from systematic changes in surface chemistry (Tx groups), the Ti branching ratio was plotted as a function of the F/O ratio obtained by XPS (Table S3), which shows no correlation (Figure S16d). The difference in Ti electron count in the two MXene systems is also found in the Ti *d*-orbital-derived DOSs obtained from DFT calculations of bare MXenes. The normalized fraction of occupied states within the valence band (-15 to 0 eV relative to the Fermi)level), also shown in Figure 2b (brown circles), indicates that the Ti bands in Ti_{2-v}V_vC have a larger fraction of occupied states than the equivalent bands in Ti_{2-v}Nb_vC. On the basis of the combined XAS and DFT results, it can be concluded that the electronic structures of the solid-solution systems are impacted by the M-site metal contribution. A similar conclusion can be drawn for the electronic contributions from V atoms as well. In the V2-yNbyCTx system, V has a

higher electron count per atom, with an average branching ratio of 0.48, compared to V in the $Ti_{2-y}V_yCT_x$ system, which has an average branching ratio of 0.45 (Figure S16e).

The electrical conductivities of bare Ti_{2-v}Nb_vC, V_{2-v}Nb_vC, and Ti_{2-v}V_vC MXene systems were calculated from multiple structures at each synthesized solid-solution concentration. This enabled a thermodynamic sampling of multiple lowenergy structures, simulating the random nature of the synthesized solid solutions. This is justified since the formation energies of each structure at a specific concentration are very close to one another (Figure S12), so the room-temperature conditions enable a fair sampling of each structure type. Details about the thermodynamic sampling are given in the Supporting Information. As shown in Figure 2c, the average electrical conductivity for Ti_{2-v}Nb_vC and Ti_{2-v}V_vC systems is predicted to increase with increasing concentrations of Nb and V, respectively. This confirms the intuition that the addition of elements with more valence electrons, and thus a higher carrier concentration, increases the conductivity of the sample. This effect is visualized with the increasing charge density between Ti₂C, TiVC, and TiNbC structures in Figure S17. The

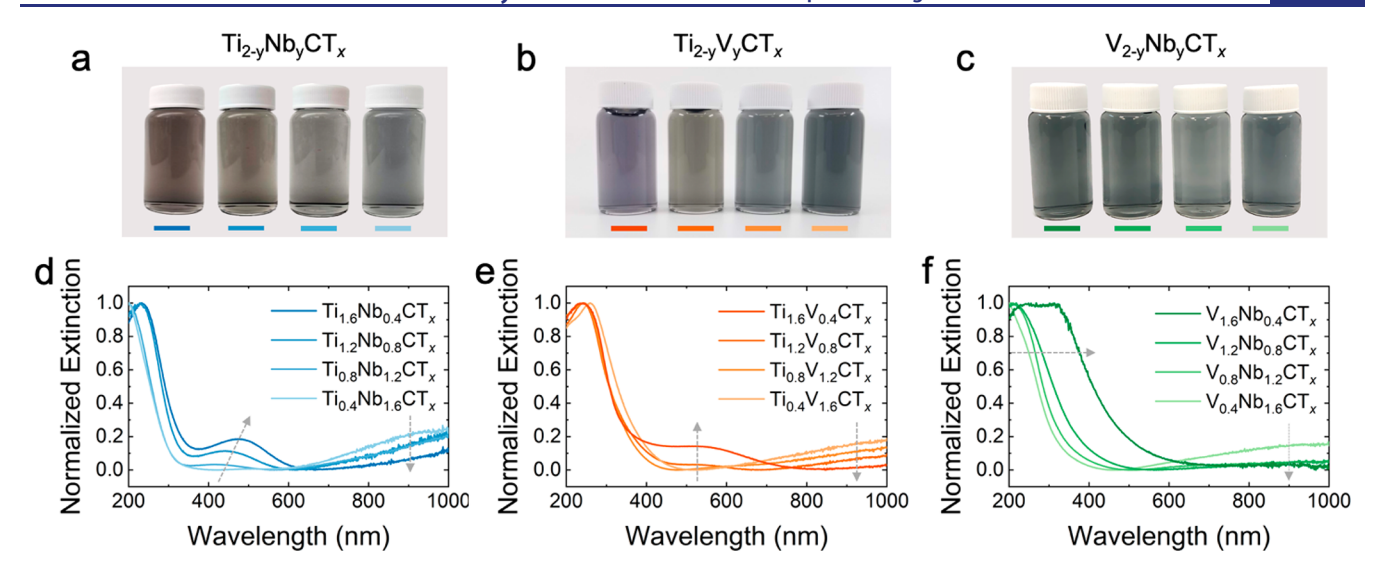


Figure 4. Optical properties of solid-solution $M'_{2-y}M''_yCT_x$ MXenes. Digital images of (a) $Ti_{2-y}Nb_yCT_x$, (b) $Ti_{2-y}V_yCT_x$, and (c) $V_{2-y}Nb_yCT_x$ colloidal solutions in deionized water. In all three systems, the gradual change in color resulting from the different stoichiometries can be observed. The quantitative UV—vis spectra normalized to a maximum extinction of 1 of the (d) $Ti_{2-y}Nb_yCT_x$, (e) $Ti_{2-y}V_yCT_x$, and (f) $V_{2-y}Nb_yCT_x$ systems. For all systems, multiple features are visible with a nonlinear shift in the absorbance with changes in the composition.

increased delocalization in TiNbC compared to TiVC illustrates that the increased delocalized electrons contribute to a higher conductivity. Further, the electrical conductivity calculations agree with the ground state DOS as a function of composition, as an increased DOS near the chemical potential is found for pure V and pure Nb states. The conductivity trend from the theoretical results obtained for bare MXenes holds for O- or F-terminated MXenes as well. We found increasing electrical conductivities calculated for Ti₂C, V₂C, and Nb₂C MXenes with terminations as detailed in Table S4.

While the calculated Ti_{2-v}Nb_vC conductivities increase almost monotonically as expected, the Ti2-vVvC and V_{2-v}Nb_vC conductivities have a curious dip in the lowconcentration region. In the Boltzmann transport theory for metals, there are two main contributions to the conductivity: the electronic DOS and the group velocity near the chemical potential.³⁹ The slight dip may occur because the Ti_{2-v}V_vC DOS at the Fermi level does not rise as sharply as the Ti_{2-v}Nb_vC DOS for increasing y values. Since this difference between V- and Nb-systems is small, however, a concurrent band structure flattening effect must be taking place for low-y Ti_{2-v}V_vC systems, which does not significantly flatten Ti_{2-y}Nb_yC band structures. A flattening of the band structure decreases the electron group velocity and thus lowers the conductivity. Further work is warranted to investigate this interesting low solid-solution concentration effect. Regardless of the root causes of the dip, the higher overall conductivity of Ti_{2-v}Nb_vC compared to Ti_{2-v}V_vC indicates that the delocalized valence electrons of Nb are important for conduction in these solid-solution systems, and that substitution in M-site can be used to significantly alter the electrical conductivity.

The electrical conductivity of the three solid-solution MXene systems was measured on vacuum-filtered films using a four-point probe method, as shown in Figure 3a. Interestingly, the relationship between the measured conductivity and M-site composition is opposite to the trend obtained from DFT calculations. For ${\rm Ti}_{2-y}{\rm Nb}_y{\rm CT}_x$ and ${\rm V}_{2-y}{\rm Nb}_y{\rm CT}_x$, the electrical conductivity decreases with increasing concentrations of Nb. In a comparison of ${\rm Ti}_{2-y}{\rm Nb}_y{\rm CT}_x$ and ${\rm Ti}_{2-y}{\rm V}_y{\rm CT}_x$ MXenes with low values of y

(Ti-rich) show higher conductivity. Ti_2CT_x and V_2CT_x show relatively high conductivity (>1000 S/cm), while that of Nb₂CT_x is low, yet DFT calculations predict that it would be among the most conductive MXenes. Temperature-dependent resistivity measurements, shown in Figure 3b-d, display a negative $d\rho/dT$, which is similar to the previous resistivity (ρ) versus temperature (T) results obtained from other double-M MXenes $(Mo_4VC_4T_x, Mo_2TiC_2T_x)$ and $Mo_2Ti_2C_3T_x)$. ^{20,41} The semiconductor-like temperature dependence could be due to a dominant role of interflake hopping processes in electronic transport or localization of charge carriers in disordered metalsite of the MXene flakes, despite the metallic nature of the MXenes. The resistivity increases with increasing Nb concentration in both $Ti_{2-y}Nb_{\nu}CT_{x}$ and $V_{2-y}Nb_{\nu}CT_{x}$ from 10 to 300 K. For the $Ti_{2-v}V_{\nu}CT_{\nu}$ system, all resistivity values are within the same order of magnitude, while a slight increase in ρ coincides with V concentration.

The significant differences between the experimentally measured and DFT-calculated conductivity trends indicate that there is a more complex combination of factors that dictates macroscopic transport than simply the metal composition (number of valence electrons), such as the surface terminations, electron scattering, or preferential defect sites. 42,43 Interflake transport or effects related to surface groups may dominate the conductivity of the film, while DFT predicts the intrinsic bare surface intraflake conductivity only. The surface element (O and F) ratios for the MXenes are different and show no clear correlation with the compositions (Table S2). This implies that different metals in solid-solution MXenes may have different preferred surface functional groups (=O, -OH, or -F). Because different etching and delamination methods were necessary for different MXenes to achieve delamination, it is difficult to directly disentangle the roles of surface terminations and M-site composition of the macroscopic electrical conductivity. Further investigation is required to better understand the connection between the Msite composition, surface chemistry, and electrical conductivity in solid-solution MXenes.

Figure 4 shows the optical properties of the solid-solution MXenes. Visually, the MXene aqueous solution color varies

from bronze to gray for Ti_{2-v}Nb_vCT_x (Figure 4a) or from purple to gray for Ti_{2-v}V_vCT_x (Figure 4b) with the chemical composition. For V_{2-y}Nb_yCT_x, both of the end compositions (Nb_2CT_r) and V_2CT_r) have characteristic absorbance peaks in the near-infrared (NIR) range, hence the minute visual differences (Figure 4c and S18). UV-vis spectroscopy was used to probe both the electronic states and quantify the optical properties, with a surface plasmon resonance (SPR) of particular relevance for MXene optical characterization. For the Ti_{2-v}Nb_vCT_r system (Figure 4d), two absorption peaks are present: one in the visible region and one in the NIR. This implies that there are two separate SPR modes available in these materials. As the amount of Ti increases, there is an emergence and red shifting of a peak in the UV-vis region. For example, this occurs at 391 and 472 nm for Ti_{0.8}Nb_{1.2}CT_x and Ti₁₆Nb₀₄CT_x, respectively. Likewise, the NIR peak (915 nm) diminishes in intensity with a decrease in Nb. The same trend is observed for Ti_{2-v}V_vCT_x (Figure 4e) and V_{2-v}Nb_vCT_x (Figure 4f). The observed peak shifts combined with color changes suggest modifications to the electronic states of each metal due to the presence of the other metal, i.e., the carrier concentration for each metal atom is being affected by its surrounding metal atoms. Furthermore, it is important to note that there are distinct optical properties of the 3 end compositions (Ti₂CT_x, V₂CT_x, and Nb₂CT_x) studied here: meaning the solid-solution MXenes, due to their multiple SPR modes, could have colors unlike any single-M MXene. Moreover, because MXenes are electrochromic, 44 we expect atomic substitution will give more diversity to the design of thin film devices. Also, conductive MXene inks of different colors can be made utilizing solid-solution MXenes. These MXenes have unique optical properties, which change in a nonlinear way as a function of composition.

CONCLUSIONS

In summary, we have systematically investigated a set of three interrelated solid-solution MXene systems (Ti_{2-v}Nb_vCT_x) $Ti_{2-v}V_{\nu}CT_{x\nu}$ and $V_{2-v}Nb_{\nu}CT_{x\nu}$), which consist of 12 MXenes of the same M₂C structure. It is demonstrated that continuous solid-solutions can be produced by M-site substitution in M₂AlC MAX phase precursors. The structure of the carbide layer of the MAX phase directly translates to the M2C MXene, and all three of these systems have random distributions of atoms in M-site position. Furthermore, it was experimentally and computationally shown that the M-site metals play a central role in changes to the electronic structure of MXenes. Solid-solution MXenes allow for unprecedented tunability and control over MXene properties by varying M-site composition, including electrical conductivity and optical absorbance. The versatility of solid-solution MXenes makes it possible to customize specific optical, mechanical, electronic, and other properties of MXenes for diverse applications.

ASSOCIATED CONTENT

Supporting Information

The Supporting Information is available free of charge at https://pubs.acs.org/doi/10.1021/jacs.0c07395.

Materials and methods; DFT calculations; XRD patterns and lattice parameters of MAX phases; EDS results and digital images of solid-solution MXene films; STEM images and EDS mappings of $Ti_{0.8}Nb_{1.2}CT_x$ and $V_{0.8}Nb_{1.2}CT_x$; EELS spectra of $Ti_{2-y}V_yCT_x$ films; XPS

spectra of Ti_{1.2}Nb_{0.8}CT_x, Ti_{1.2}V_{0.8}CT_x, and V_{1.2}Nb_{0.8}CT_x; XAS spectra of solid-solution MXenes (PDF)

AUTHOR INFORMATION

Corresponding Author

Yury Gogotsi — A. J. Drexel Nanomaterials Institute and Department of Materials Science and Engineering, Drexel University, Philadelphia, Pennsylvania 19104, United States; orcid.org/0000-0001-9423-4032; Email: gogotsi@drexel.edu

Authors

Meikang Han − A. J. Drexel Nanomaterials Institute and Department of Materials Science and Engineering, Drexel University, Philadelphia, Pennsylvania 19104, United States; orcid.org/0000-0003-3309-988X

Kathleen Maleski — A. J. Drexel Nanomaterials Institute and Department of Materials Science and Engineering, Drexel University, Philadelphia, Pennsylvania 19104, United States;
○ orcid.org/0000-0003-4032-7385

Christopher Eugene Shuck — A. J. Drexel Nanomaterials Institute and Department of Materials Science and Engineering, Drexel University, Philadelphia, Pennsylvania 19104, United States; ⊚ orcid.org/0000-0002-1274-8484

Yizhou Yang — Department of Materials Science and Engineering, Drexel University, Philadelphia, Pennsylvania 19104, United States

James T. Glazar – Department of Materials Science and Engineering, University of Pennsylvania, Philadelphia, Pennsylvania 19104, United States

Alexandre C. Foucher — Department of Materials Science and Engineering, University of Pennsylvania, Philadelphia, Pennsylvania 19104, United States; orcid.org/0000-0001-5042-4002

Kanit Hantanasirisakul — A. J. Drexel Nanomaterials Institute and Department of Materials Science and Engineering, Drexel University, Philadelphia, Pennsylvania 19104, United States; orcid.org/0000-0002-4890-1444

Asia Sarycheva — A. J. Drexel Nanomaterials Institute and Department of Materials Science and Engineering, Drexel University, Philadelphia, Pennsylvania 19104, United States

Nathan C. Frey — Department of Materials Science and Engineering, University of Pennsylvania, Philadelphia, Pennsylvania 19104, United States; orcid.org/0000-0001-5291-6131

Steven J. May — Department of Materials Science and Engineering, Drexel University, Philadelphia, Pennsylvania 19104. United States

Vivek B. Shenoy – Department of Materials Science and Engineering, University of Pennsylvania, Philadelphia, Pennsylvania 19104, United States

Eric A. Stach — Department of Materials Science and Engineering, University of Pennsylvania, Philadelphia, Pennsylvania 19104, United States; orcid.org/0000-0002-3366-2153

Complete contact information is available at: https://pubs.acs.org/10.1021/jacs.0c07395

Author Contributions

\$These authors contributed equally to this work.

Notes

The authors declare no competing financial interest.

ACKNOWLEDGMENTS

Synthesis and experimental characterization of MXenes was supported by the U.S. Department of Energy (DoE), Office of Science, Office of Basic Energy Sciences, grant #DESC0018618. We gratefully acknowledge Dr. John William Freeland for assistance with XAS measurements, which were performed at beamline 4-ID-C at the Advanced Photon Source. This research used resources of the Advanced Photon Source, a U.S. DoE Office of Science User Facility operated for the DoE Office of Science by Argonne National Laboratory under Contract No. DE-AC02-06CH11357. V.B.S. acknowledges support from the U.S. National Science Foundation, grants EFMA-542879 and CMMI-1727717, and the Army Research Office by contract W911NF-16-1-0447 for DFT calculations. N.C.F. was supported by the Department of Defense (DoD) through the National Defense Science & Engineering Graduate Fellowship (NDSEG) Program. A.C.F. and E.A.S. would like to acknowledge the Vagelos Institute for Energy Science and Technology at the University of Pennsylvania for a graduate fellowship. This work was performed in part at the Singh Center for Nanotechnology at the University of Pennsylvania, a member of the National Nanotechnology Coordinated Infrastructure (NNCI) network, which is supported by the National Science Foundation (Grant NNCI-1542153) and to the Nanoscale Characterization Facility, supported by in part through the University of Pennsylvania Materials Research Science and Engineering Center (MRSEC) (DMR-1720530). XRD, XPS, and SEM-EDS analyses were performed using instruments in the Materials Characterization Core at Drexel University. We thank Dr. Narendra Kurra for the help with collecting Raman spectra and Dr. Mikhail Shekhirev for the assistance with UVvis spectroscopy measurements.

■ REFERENCES

- (1) Sarker, P.; Harrington, T.; Toher, C.; Oses, C.; Samiee, M.; Maria, J. P.; Brenner, D. W.; Vecchio, K. S.; Curtarolo, S. High-Entropy High-Hardness Metal Carbides Discovered by Entropy Descriptors. *Nat. Commun.* **2018**, *9*, 4980.
- (2) Gusev, A.; Rempel, A., in *Materials Science of Carbides, Nitrides and Borides*. Gogotsi, Y.; Andrievski, R., Eds.; Kluwer Academic: Dordrecht, 1999; pp 47–64.
- (3) Lei, Z.; Liu, X.; Wu, Y.; Wang, H.; Jiang, S.; Wang, S.; Hui, X.; Wu, Y.; Gault, B.; Kontis, P. Enhanced Strength and Ductility in a High-Entropy Alloy *via* Ordered Oxygen Complexes. *Nature* **2018**, 563, 546
- (4) Ye, R.; Del Angel-Vicente, P.; Liu, Y.; Arellano-Jimenez, M. J.; Peng, Z.; Wang, T.; Li, Y.; Yakobson, B. I.; Wei, S. H.; Yacaman, M. J. High-Performance Hydrogen Evolution from $MoS_{2(1-x)}P_x$ Solid Solution. *Adv. Mater.* **2016**, 28, 1427–1432.
- (5) Uematsu, T.; Doi, T.; Torimoto, T.; Kuwabata, S. Preparation of Luminescent AgInS₂–AgGaS₂ Solid Solution Nanoparticles and Their Optical Properties. *J. Phys. Chem. Lett.* **2010**, *1*, 3283–3287.
- (6) Li, H.; Duan, X.; Wu, X.; Zhuang, X.; Zhou, H.; Zhang, Q.; Zhu, X.; Hu, W.; Ren, P.; Guo, P. Growth of Alloy MoS_{2x}Se_{2(1-x)} Nanosheets with Fully Tunable Chemical Compositions and Optical Properties. *J. Am. Chem. Soc.* **2014**, *136*, 3756–3759.
- (7) Bandyopadhyay, D.; Sharma, R.; Chakraborti, N. The C-Nb-Ti System (Carbon-Niobium-Titanium). *J. Phase Equilib.* **2000**, *21*, 102. (8) Zhang, W.; Peng, Y.; Du, Y.; Chen, L.; Li, Y.; Wang, S.; Wen, G.; Xie, W. A Thermodynamic Description of the C–Ti–V System over

- the Whole Composition and Temperature Ranges. *Int. J. Refract. Hard Met.* **2015**, *48*, 346–354.
- (9) Frisk, K. Thermodynamic Modelling of Multicomponent Cubic Nb, Ti and V Carbides/Carbonitrides. *CALPHAD: Comput. Coupling Phase Diagrams Thermochem.* **2008**, 32, 326–337.
- (10) Barsoum, M. W. MAX Phases: Properties of Machinable Ternary Carbides and Nitrides. Wiley-VCH: Weinheim, 2013; pp 1–10.
- (11) Sokol, M.; Natu, V.; Kota, S.; Barsoum, M. W. On the Chemical Diversity of the MAX Phases. *Trends Chem.* **2019**, *1*, 210–223.
- (12) Caspi, E. A. N.; Chartier, P.; Porcher, F.; Damay, F.; Cabioc'h, T. Ordering of (Cr,V) Layers in Nanolamellar $(Cr_{0.5}V_{0.5})_{n+1}AlC_n$ Compounds. *Mater. Res. Lett.* **2015**, 3, 100–106.
- (13) Zapata-Solvas, E.; Hadi, M. A.; Horlait, D.; Parfitt, D. C.; Thibaud, A.; Chroneos, A.; Lee, W. E. Synthesis and Physical Properties of $(Zr_{1-x}, Ti_x)_3AlC_2$ MAX Phases. *J. Am. Ceram. Soc.* **2017**, 100, 3393–3401.
- (14) Cabioch, T.; Eklund, P.; Mauchamp, V.; Jaouen, M.; Barsoum, M. W. Tailoring of the Thermal Expansion of $Cr_2(Al_xGe_{1-x})C$ Phases. *J. Eur. Ceram. Soc.* **2013**, *33*, 897–904.
- (15) Li, Y.; Lu, J.; Li, M.; Chang, K.; Zha, X.; Zhang, Y.; Chen, K.; Persson, P. O. Å.; Hultman, L.; Eklund, P.; Du, S.; Francisco, J. S.; Chai, Z.; Huang, Z.; Huang, Q. Multielemental Single—Atom—Thick A Layers in Nanolaminated $V_2(Sn,A)C$ (A = Fe, Co, Ni, Mn) for Tailoring Magnetic Properties. *Proc. Natl. Acad. Sci. U. S. A.* **2020**, 117, 820–825.
- (16) Meng, F.; Zhou, Y.; Wang, J. Strengthening of Ti₂AlC by Substituting Ti with V. Scr. Mater. 2005, 53, 1369–1372.
- (17) Lin, S.; Huang, Y.; Zu, L.; Kan, X.; Lin, J.; Song, W.; Tong, P.; Zhu, X.; Sun, Y. Alloying Effects on Structural, Magnetic, and Electrical/Thermal Transport Properties in MAX-Phase $\text{Cr}_{2-x}\text{M}_x\text{GeC}$ (M = Ti, V, Mn, Fe, and Mo). *J. Alloys Compd.* **2016**, 680, 452–461.
- (18) Gogotsi, Y.; Anasori, B. The Rise of MXenes. ACS Nano 2019, 13, 8491-8494.
- (19) Naguib, M.; Kurtoglu, M.; Presser, V.; Lu, J.; Niu, J.; Heon, M.; Hultman, L.; Gogotsi, Y.; Barsoum, M. W. Two-Dimensional Nanocrystals Produced by Exfoliation of Ti₃AlC₂. *Adv. Mater.* **2011**, 23, 4248–4253.
- (20) Deysher, G.; Shuck, C. E.; Hantanasirisakul, K.; Frey, N. C.; Foucher, A. C.; Maleski, K.; Sarycheva, A.; Shenoy, V. B.; Stach, E. A.; Anasori, B.; Gogotsi, Y. Synthesis of Mo₄VAlC₄ MAX Phase and Two-Dimensional Mo₄VC₄ MXene with 5 Atomic Layers of Transition Metals. *ACS Nano* **2020**, *14*, 204–217.
- (21) Wang, Y.; Zheng, W.; Zhang, P.; Tian, W.; Chen, J.; Sun, Z. Preparation of $(V_x, Ti_{1-x})_2C$ MXenes and Their Performance as Anode Materials for LIBs. *J. Mater. Sci.* **2019**, *54*, 11991–11999.
- (22) Yang, J.; Naguib, M.; Ghidiu, M.; Pan, L. M.; Gu, J.; Nanda, J.; Halim, J.; Gogotsi, Y.; Barsoum, M. W. Two-Dimensional Nb-Based M₄C₃ Solid Solutions (MXenes). *J. Am. Ceram. Soc.* **2016**, *99*, 660–666.
- (23) Wang, Z.; Zhang, X.; Ren, Z.; Liu, Y.; Hu, J.; Li, H. W.; Gao, M.; Pan, H.; Liu, Y. In Situ Formed Ultrafine NbTi Nanocrystals from a NbTiC Solid-Solution MXene for Hydrogen Storage in MgH₂. *J. Mater. Chem. A* **2019**, *7*, 14244–14252.
- (24) Naguib, M.; Mashtalir, O.; Carle, J.; Presser, V.; Lu, J.; Hultman, L.; Gogotsi, Y.; Barsoum, M. W. Two-Dimensional Transition Metal Carbides. *ACS Nano* **2012**, *6*, 1322–1331.
- (25) Yazdanparast, S.; Soltanmohammad, S.; Fash White, A.; Tucker, G. J.; Brennecka, G. L. Synthesis and Surface Chemistry of 2D TiVC Solid-Solution MXenes. ACS Appl. Mater. Interfaces 2020, 12, 20129–20137.
- (26) Pinto, D.; Anasori, B.; Avireddy, H.; Shuck, C. E.; Hantanasirisakul, K.; Deysher, G.; Morante, J. R.; Porzio, W.; Alshareef, H. N.; Gogotsi, Y. Synthesis and Electrochemical Properties of 2D Molybdenum Vanadium Carbides—Solid Solution MXenes. *J. Mater. Chem. A* **2020**, *8*, 8957—8968.
- (27) Ling, Z.; Simon, P., in 2D Metal Carbides and Nitrides (MXenes). Anasori, B.; Gogotsi, Y., Eds., Springer: Cham, 2019; pp 349–457.

- (28) Sarycheva, A.; Polemi, A.; Liu, Y.; Dandekar, K.; Anasori, B.; Gogotsi, Y. 2D Titanium Carbide (MXene) for Wireless Communication. *Sci. Adv.* **2018**, *4*, eaau0920.
- (29) Wang, X.; Mathis, T. S.; Li, K.; Lin, Z.; Vlcek, L.; Torita, T.; Osti, N. C.; Hatter, C.; Urbankowski, P.; Sarycheva, A.; Tyagi, M.; Mamontov, E.; Simon, P.; Gogotsi, Y. Influences from Solvents on Charge Storage in Titanium Carbide MXenes. *Nat. Energy* **2019**, *4*, 241–248.
- (30) Zhang, J.; Zhao, Y.; Guo, X.; Chen, C.; Dong, C. L.; Liu, R. S.; Han, C. P.; Li, Y.; Gogotsi, Y.; Wang, G. Single Platinum Atoms Immobilized on an MXene as an Efficient Catalyst for the Hydrogen Evolution Reaction. *Nat. Catal.* **2018**, *1*, 985–992.
- (31) Shuck, C. E.; Sarycheva, A.; Anayee, M.; Levitt, A.; Zhu, Y.; Uzun, S.; Balitskiy, V.; Zahorodna, V.; Gogotsi, O.; Gogotsi, Y. Scalable Synthesis of Ti₃C₂T_x MXene. *Adv. Eng. Mater.* **2020**, 22, 1901241.
- (32) Han, M.; Shuck, C. E.; Rakhmanov, R.; Parchment, D.; Anasori, B.; Koo, C. M.; Friedman, G.; Gogotsi, Y. Beyond Ti₃C₂T_x: MXenes for Electromagnetic Interference Shielding. *ACS Nano* **2020**, *14*, 5008–5016.
- (33) Sarycheva, A.; Gogotsi, Y. Raman Spectroscopy Analysis of the Structure and Surface Chemistry of Ti₃C₂T_x MXene. *Chem. Mater.* **2020**, 32, 3480–3488.
- (34) Van De Walle, A.; Asta, M.; Ceder, G., The Alloy Theoretic Automated Toolkit: A User Guide. 2002, arXiv preprint: cond-mat/0212159
- (35) Yang, Y.; Hantanasirisakul, K.; Frey, N. C.; Anasori, B.; Green, R. J.; Rogge, P. C.; Waluyo, I.; Hunt, A.; Shafer, P.; Arenholz, E.; Shenoy, V. B.; Gogotsi, Y.; May, S. J. Distinguishing Electronic Contributions of Surface and Sub-Surface Transition Metal Atoms in Ti-Based MXenes. 2D Mater. 2020, 7, 025015.
- (36) Crocombette, J.; Jollet, F. Ti 2p X-Ray Absorption in Titanium Dioxides (TiO_2): the Influence of the Cation Site Environment. *J. Phys.: Condens. Matter* **1994**, *6*, 10811.
- (37) Kalavathi, S.; Amirthapandian, S.; Chandra, S.; Sahu, P. C.; Sahu, H. Valence State, Hybridization and Electronic Band Structure in the Charge Ordered AlV₂O₄. *J. Phys.: Condens. Matter* **2014**, *26*, 015601.
- (38) Bach, D.; Schneider, R.; Gerthsen, D.; Verbeeck, J.; Sigle, W. EELS of Niobium and Stoichiometric Niobium-Oxide Phases—Part I: Plasmon and Near-Edges Fine Structure. *Microsc. Microanal.* **2009**, *15*, 505–523.
- (39) Madsen, G. K.; Carrete, J.; Verstraete, M. J. BoltzTraP2, a Program for Interpolating Band Structures and Calculating Semi-Classical Transport Coefficients. *Comput. Phys. Commun.* **2018**, 231, 140–145.
- (40) Khazaei, M.; Arai, M.; Sasaki, T.; Estili, M.; Sakka, Y. Two-Dimensional Molybdenum Carbides: Potential Thermoelectric Materials of the MXene Family. *Phys. Chem. Chem. Phys.* **2014**, *16*, 7841–7849.
- (41) Anasori, B.; Shi, C.; Moon, E. J.; Xie, Y.; Voigt, C. A.; Kent, P. R.; May, S. J.; Billinge, S. J.; Barsoum, M. W.; Gogotsi, Y. Control of Electronic Properties of 2D Carbides (MXenes) by Manipulating Their Transition Metal Layers. *Nanoscale Horiz.* **2016**, *1*, 227–234.
- (42) Guo, Z.; Miao, N.; Zhou, J.; Pan, Y.; Sun, Z. Coincident Modulation of Lattice and Electron Thermal Transport Performance in MXenes via Surface Functionalization. *Phys. Chem. Chem. Phys.* **2018**, 20, 19689–19697.
- (43) Wu, H.; Guo, Z.; Zhou, J.; Sun, Z. Vacancy-Mediated Lithium Adsorption and Diffusion on MXene. *Appl. Surf. Sci.* **2019**, 488, 578–585.
- (44) Salles, P.; Pinto, D.; Hantanasirisakul, K.; Maleski, K.; Shuck, C. E.; Gogotsi, Y. Electrochromic Effect in Titanium Carbide MXene Thin Films Produced by Dip-Coating. *Adv. Funct. Mater.* **2019**, 29, 1809223.